01 Jan 2020

Direct Numerical Simulation Of Turbulent Pressure Fluctuations Over A Cone At Mach 8

Junji Huang

Lian Duan
Missouri Unviersity of Science and Technology, duanl@mst.edu

Katya M. Casper

Ross M. Wagnild

et. al. For a complete list of authors, see *https://scholarsmine.mst.edu/mec_aereng_facwork/5442*

Recommended Citation

Direct Numerical Simulation of Turbulent Pressure Fluctuations over a Cone at Mach 8

Junji Huang* and Lian Duan[†]
The Ohio State University, Columbus, OH 43210, USA

Katya M. Casper[‡], Ross M. Wagnild[§], and Neal P. Bitter[¶]
Sandia National Laboratories, Albuquerque, NM 87185, USA

Direct numerical simulations (DNS) were conducted to characterize the pressure fluctuations under the turbulent portion of the boundary layer over a sharp $7°$ half-angle cone at a nominal freestream Mach number of 8 and a unit Reynolds number of $Re_{unit} = 13.4 \times 10^6 / m$. The axisymmetric cone geometry and the flow conditions of the DNS matched those measured in the Sandia Hypersonic Wind Tunnel at Mach 8 (Sandia HWT-8). The DNS-predicted wall pressure statistics, including the root-mean-square (r.m.s.) fluctuations and the power spectral density (PSD), were compared with those measured in the Sandia HWT-8. A good comparison between the DNS and the experiment was shown for the r.m.s. and PSD of wall-pressure fluctuations after spatial averaging was applied to the DNS data over an area similar to the sensing area of the transducer. The finite size of the PCB132 transducer, with a finite sensing area of $d^+ \approx 50$, caused significant spectral attenuation at high frequencies in the experimentally measured PSD, and the loss in sensor resolution resulted in an approximately 27% reduction in r.m.s. pressure fluctuations. The attenuation due to finite sensor sizes has only a small influence on wall-pressure coherence, as indicated by the good comparisons between the DNS without spatial filtering and the experiment for transducers with either streamwise or spanwise separations. The characteristics of turbulent pressure fluctuations at the cone surface were also compared with those over a flat plate and at the wind-tunnel nozzle wall to assess the effect of flow configurations on the scaling relations of turbulent pressure fluctuations. The inner scale was found to successfully collapse wall-pressure PSD of the cone with those over a nozzle wall and on a flat plate at a similar freestream Mach number. For all the three flow configurations, the Corcos model was found to deliver good predictions of wall pressure coherence over intermediate and high frequencies, and the Corcos parameters for the streamwise and spanwise coherence at Mach 8 were found to be similar to those reported in the literature at lower supersonic Mach numbers.

I. Nomenclature

C_f	=	Skin friction coefficient, $C_f = \tau_w / (0.5\rho_e U_e^2)$, dimensionless
C_p	=	heat capacity at constant pressure, J/(K·kg)
C_v	=	heat capacity at constant volume, J/(K·kg)
H	=	shape factor, $H = \delta^*/\theta$, dimensionless
M	=	Mach number, dimensionless
Pr	=	Prandtl number, $Pr = 0.71$, dimensionless
R	=	ideal gas constant, $R = 287$, J/(K·kg), m
Re_θ	=	Reynolds number based on momentum thickness and edge viscosity, $Re_\theta \equiv \frac{\rho_e U_e \theta}{\mu_e}$,
	=	dimensionless
Re_{δ_2}	=	Reynolds number based on momentum thickness and wall viscosity, $Re_{\delta_2} \equiv \frac{\rho_e U_e \theta}{\mu_w}$, dimensionless

*Graduate Student, Department of Mechanical and Aerospace Engineering

[†]Associate Professor, Department of Mechanical and Aerospace Engineering, Senior Member, AIAA.

[‡]Principal Member of the Technical Staff. Senior Member AIAA.

[§]Principal Member of the Technical Staff. Senior Member AIAA.

[¶]Principal Member of the Technical Staff. Senior Member AIAA.

1

Re_τ	=	Reynolds number based on shear velocity and wall viscosity, $Re_\tau \equiv \frac{\rho_w u_\tau \delta}{\mu_w}$, dimensionless
T	=	temperature, K
T_o	=	total temperature, K
T_r	=	recovery temperature, $T_r = T_e(1 + 0.89 * \frac{\gamma-1}{2} M_e^2)$, K
U_c	=	propagation speed of wall pressure fluctuations, m/s
U_∞	=	freestream velocity, m/s
a	=	speed of sound, m/s
p	=	pressure, Pa
q	=	dynamic pressure, Pa
r	=	radial coordinate, m
u	=	streamwise velocity, m/s
u_τ	=	friction velocity, $u_\tau \equiv \sqrt{\tau_w/\bar{\rho}_w}$, m/s
v	=	spanwise velocity, m/s
w	=	wall-normal velocity, m/s
x	=	streamwise direction of the right hand Cartesian coordinate
y	=	spanwise direction of the right hand Cartesian coordinate
z	=	wall-normal direction of the right hand Cartesian coordinate
z_τ	=	viscous length, $z_\tau = \nu_w/u_\tau$, m
γ	=	specific heat ratio, $\gamma = C_p/C_v$, dimensionless
δ	=	boundary layer thickness (based on 99.5% of the total enthalpy), m
δ^*	=	displacement thickness, $\int_0^\delta \left(1 - \frac{\rho U}{\rho_e U_e}\right) dz$, m
κ	=	thermal conductivity, $\kappa = \mu C_p/Pr$, W/(m·K)
θ	=	momentum thickness, $\int_0^\delta \frac{\rho U}{\rho_e U_e} \left(1 - \frac{U}{U_e}\right) dz$, m
μ	=	dynamic viscosity, kg/(m·s)
ν	=	kinematic viscosity, $\nu = \mu/\rho$, m²·s
ρ	=	density, kg/m³
τ_w	=	wall shear stress, Pa
	=	
Subscripts	=	
e	=	boundary-layer edge variables
i	=	inflow station for the domain of direct numerical simulations
o	=	stagnation quantities
rms	=	root mean square
w	=	wall variables
∞	=	freestream variables
	=	
Superscripts	=	
+	=	inner wall units
$\overline{(\cdot)}$	=	averaged variables
$(\cdot)'$	=	perturbation from averaged variable

II. Introduction

One of the primary sources of vibratory loading during atmospheric reentry is the wall-pressure fluctuations induced by hypersonic transitional and turbulent boundary layers. These pressure fluctuations can be intense enough to cause severe vibration of internal components and lead to damaging effects such as flutter. Characterizing this fluctuating pressure on vehicle surfaces is thus of practical importance to the structural design of hypersonic vehicles. So far, there is a lack of physics-based models that can adequately predict the magnitude, frequency content, location, and spatial extent of boundary-layer-induced pressure fluctuations at hypersonic speeds. The lack of predictive capability leads to heavier vehicles and degraded flight performance.

To improve prediction of hypersonic pressure fluctuations, experiments were conducted on a 7° sharp cone at zero angle of attack under noisy flow in the Sandia National Laboratories Hypersonic Wind Tunnel (HWT) at Mach 5, 8, and

14 [1, 2]. The measured pressure loading on the cone sidewall was compared to that on wind tunnel walls at similar Mach numbers for developing statistical pressure fluctuation model [3]. The comparison showed that the measured pressure power spectral densities (PSD) for hypersonic flow over a sharp 7° half-angle cone at freestream Mach numbers of 5.0 and 7.9 have much higher magnitude than wind tunnel wall data at similar Mach numbers. The causes for the observed differences are largely unknown. As far as the development of reduced-order turbulent boundary layer pressure fluctuation models is concerned, a semi-empirical model proposed by Smith et al. [3] compares fairly well with the wind tunnel wall data, but predicts the cone pressure fluctuations at least an order of magnitude lower than the experimental measurements. A more accurate characterization of the cone flow field is thus needed to better calibrate model parameters and to reduce uncertainties associated with boundary-layer edge scaling parameters.

The current work aims to complement the aforementioned experimental and modeling efforts by direct numerical simulations (DNS) of a turbulent boundary layer over a sharp hypersonic cone, with the freestream conditions and cone geometry representative of the experiments at Sandia HWT-8. The DNS allowed comparisons to the cone experiments at the same flow conditions and also provided access to multipoint pressure statistics and pressure structures that cannot be measured easily. Additionally, the computed turbulent pressure fluctuations over the cone surface were compared to those on the nozzle wall of the Sandia HWT-8 as well as over a canonical flat plate at a similar freestream Mach number. Such comparisons help characterize scaling relations of fluctuating pressure field and their association with boundary-layer parameters. They also shed light on differences in the fluctuating pressure field between different configurations.

The paper is structured as follows. The flow conditions and numerical methods are outlined in Section III. Section IV presents DNS results of hypersonic turbulent boundary layer over a sharp 7° half-angle cone, including the comparison of the DNS with the experiments in the Sandia HWT-8 (Section IV.A) and the investigation of flow configurations on wall-pressure statistics (Section IV.B). A summary of the work is given in Section V.

III. Flow Conditions and DNS Methodology

DNS of hypersonic turbulent boundary layers were conducted over a 0.517-m-long, 7° half-angle cone with a sharp nose radius of 0.05 mm. The axisymmetric cone configuration matched that of the cone experiment in Sandia HWT-8 [1, 2]. Targeted freestream conditions within the DNS are summarized in Table 1, which fall within the range of operational conditions of the Sandia HWT-8. At a selected Reynolds number of $Re_{unit} = 13.4 \times 10^6/m$, experiments have confirmed that the aft portion of the cone ($x \gtrsim 0.3$) is under a fully turbulent boundary layer [1], where x is the axial distance from the sharp nose. The wall temperature of the cone is 298 K, corresponding to a wall-to-total temperature ratio of $T_w/T_o \approx 0.48$.

Table 1   Nominal freestream conditions for the DNS of a Mach 8 turbulent boundary layer over a 7° half-angle cone with a sharp nose.

M_∞	P_o (kPa)	T_o (K)	Re_{unit} (1/m)	T_w (K)
7.91	4692	617	13.4×10^6	298

A. Governing Equations and Numerical Methods

To simulate the turbulent boundary layer on a circular cone as that used in the experiments in Sandia HWT-8, the full three-dimensional compressible Navier-Stokes equations in conservation form were solved numerically in cylindrical coordinates. The working fluid was nitrogen and fell within the perfect gas regime. The usual constitutive relations for a Newtonian fluid were used: the viscous stress tensor was linearly related to the rate-of-strain tensor, and the heat flux vector was linearly related to the temperature gradient through Fourier's law. The coefficient of viscosity μ was computed from Keyes law [4], and the coefficient of thermal conductivity κ was computed from $\kappa = \mu C_p/Pr$, with the molecular Prandtl number $Pr = 0.71$. The inviscid fluxes of the governing equations were computed using a seventh-order weighted essentially non-oscillatory (WENO) scheme [5]. The viscous fluxes were discretized using a fourth-order central difference scheme and time integration was performed using a third-order low-storage Runge-Kutta scheme [6].

The details of the DNS methodology have been documented in our previous simulations of supersonic and hypersonic turbulent boundary layers [7–12].

3

B. Simulation Setup and Boundary Conditions

To set up the DNS of flow over a circular cone, a precursor RANS simulation was first conducted using the ANSYS Fluent code [13] for initializing the DNS Case and for providing boundary conditions for the principal DNS. As seen in Figure 1a, the RANS calculation simulates the full cone geometry that included the cone nose region and the leading-edge shock of the cone. The RANS domain extended from $x = -0.11$ mm to approximately the cone base at $x = 0.517$ m in the axial direction. The wall-normal extent of the grid increased down the length of the cone, from 0.06 mm at the tip to 47 mm at the base, allowing for the shock to be fully contained within the grid. The outer boundary that lay outside the shock followed a hyperbola, which is similar to the shock shape. A two-dimensional computational grid was generated using generalized curvilinear coordinates (i,k), representing downstream and wall-normal coordinates, respectively. The grid was stretched in the wall-normal (k) direction and clustered close to the wall. In the downstream (i) direction, the grid was clustered near the nose and was uniform in the flat afterbody region. Given that the cone is positioned at zero angle of attack, the flow was assumed to be axisymmetric. Calculations were performed using a grid of 5001×400 grid points. The adequacy of the grid resolution was monitored by examining mean flow solutions to ensure that at least 120 points normal to the cone surface were placed in the boundary layer, and that the nondimensional wall distance z^+ for the grid, extracted from the converged RANS solution, was everywhere less than one ($z^+ < 1$), where z^+ was used as a measure of local grid quality at the wall in the wall-normal direction. The flow was assumed to be fully turbulent throughout the cone (i.e., with turbulence model switched on from the nose); and the Reynolds stresses and turbulent heat flux were modeled via Menter's SST model with a constant turbulent Prandtl number of 0.85. A difference of less than 10% in mean flow field solution was shown when comparing transition onset from the nosetip against transition onset modeled at 0.14 m, the location predicted by linear stability theory [3]. The mean and Reynolds-stress profiles of the RANS were extracted at the DNS inflow location and used during the DNS.

The domain of the DNS (Case Cone_x0p15 shown in Figure 1b) started downstream of the nose at $x = 0.15$ m, which is significantly upstream of the reference sensor location ($x = 0.396$ m, or $\Delta L/\delta \approx 83$) where a turbulent boundary layer was measured in experiments [1, 3]. Previous experience showed that such a selection of the DNS inflow location could minimize any artificial effects of inflow turbulence generation and virtually guarantee the convergence of high-order turbulence statistics at the downstream locations where these statistics are collected. The outflow of the DNS was positioned downstream of the cone base at $x = 0.58$ m to ensure that the downstream portion of cone is free of any potential influence of outflow boundary condition. The insensitivity of flow statistics to inflow and outflow boundary conditions was further assessed by comparing the DNS results with those of a second DNS (Case Cone_x0p20 shown in Figure 1c) computed with different inflow and outflow boundary locations, and such an assessment will be discussed in Section III.C. The top boundary of the DNS domain was located above the oblique shock emanating from the nose of the cone, as visualized in Figure 1a, which is similar to that of a previous DNS by Sivasubramanian and Fasel who studied hypersonic boundary-layer transition over a cone [14].

In the DNS of turbulent flow over a circular cone, the non-uniform digital-filtering (DF) method [15, 16] was applied to generate inflow turbulence for the DNS, with the mean boundary layer profiles and the Reynolds stress tensor at the inflow provided by the pre-cursor RANS. The robustness and adequacy of the DF inflow method for predicting the global turbulence field within hypersonic turbulent boundary layers has been demonstrated in our prior work for both flat plate [16] and axisymmetric nozzle [9, 12, 17] configurations. On the cone surface, no-slip conditions were applied for the three velocity components, and an isothermal condition was used for the temperature with $T_w = 298$ K. At the outflow boundary, unsteady nonreflecting boundary conditions based on Thompson [18] was imposed after introducing an outflow zone with a gradually stretched axial grid beyond the physical end of the cone. A sponge region was imposed at the top boundary of the simulation domain in which the flow is forced towards the freestream condition. Given the axisymmetric nature of a circular cone, the DNS domain included only a portion of the full azimuthal circumference, with periodic boundary conditions prescribed at the azimuthal boundaries. The azimuthal domain size, as denoted to be ϕ in Figure 1b, was selected to be 16.9°, which corresponds to an azimuthal length along the cone surface of approximately 4.6δ, where δ is the boundary-layer thickness at the reference sensor location ($x = 0.396$ m). Details of the grid dimensions, domain size, and resolutions of the DNS are listed in Table 2. The selection of grid and other aspects of the numerical solution was based on extensive experience with a similar class of flows. Spot checks were made to ensure that the impact of reasonable variations with respect to those choices is negligible.

C. Assessment of DNS Data

Previous DNS of spatially-developing turbulent boundary layers in the incompressible and supersonic Mach number regimes have shown that the use of very long streamwise domains is required for boundary layer turbulence to recover

(a)

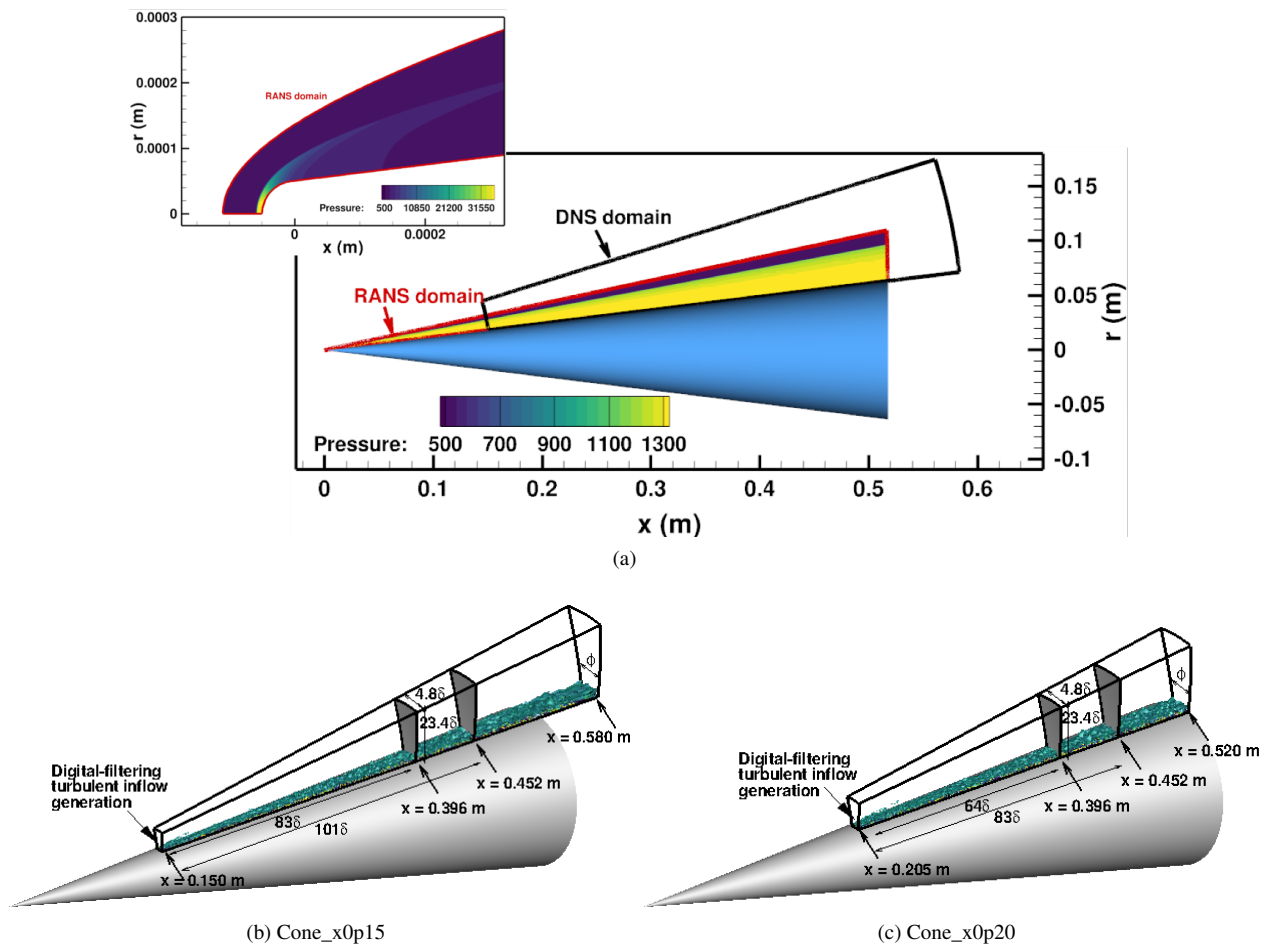(b) Cone_x0p15

(c) Cone_x0p20

Fig. 1   Computational domain and simulation setup for DNS of hypersonic flows over a cone, with the axisymmetric cone geometry and the flow conditions of the DNS match those measured in Sandia HWT-8. The instantaneous flow is shown by the isosurface of the magnitude of the density gradient. δ is the boundary-layer thickness at the reference sensor location $x = 0.396$ m.

Table 2   Domain size and grid resolution for DNS cases.

Case	x_{range}, m	ϕ (deg)	$N_x \times N_\theta \times N_r$	Δx^+	Δy_w^+	Δy_e^+	Δr_w^+	Δr_e^+
Cone_x0p15	$0.15 - 0.580$	16.9	$3840 \times 160 \times 200$	5.2	4.6	4.8	0.45	4.4
Cone_x0p20	$0.205 - 0.520$	16.9	$3072 \times 160 \times 200$	5.2	4.7	5.0	0.44	4.5
DNS SPARC	$0.0002 - 0.542$	30.0	$8600 \times 460 \times 700$	3.93	2.69	2.83	0.35	0.59

from the initial transient due to inflow turbulence generation techniques and achieve a fully developed equilibrium state, which makes a highly reliable spatial simulation extremely demanding. To ensure that the current DNS achieves a fully developed equilibrium state of a turbulent boundary layer in the downstream portion of the computational box, a second DNS (Case Cone_x0p2) was conducted with a different streamwise extent of the computation domain (0.205 m ≤ x ≤ 0.520 m) while keeping other simulation parameters identical as Case Cone_x0p15. Simulating the same flow with an identical set-up except for the inflow and outflow locations warrants proper comparability and allows for a highly reliable quantitative evaluation of the "useful" streamwise or Reynolds number ranges covered by the selected DNS domain. The two WENO DNS runs with different simulation domains are referred to as Cases Cone_x0p15 and Cone_x0p2 in Table 2.

In conjunction with the aforementioned Cases Cone_x0p15 and Cone_x0p2 that were run using a high-order finite difference WENO code as described in Section III.A, a third DNS of Mach 8 turbulent flow over the Sandia cone was conducted using the Sandia Parallel Aerodynamics and Reentry Code (SPARC), which is a shock-capturing CFD code under development at Sandia National Laboratories. This code is designed to run on next-generation computing architectures and scale efficiently on exascale-class computing platforms. SPARC supports a variety of numerical schemes for hypersonic flow simulation, but in this work it operates as a cell-centered finite volume code. In order to conduct compressible turbulence simulations, the code uses the kinetic energy consistent finite volume scheme developed by Subbareddy and Candler [19]. The time advancement scheme is a 2nd-order implicit method based on the point-Jacobi, backward difference formula. The turbulent DNS carried out using the SPARC code mirrored Cases Cone_x0p15 and Cone_x0p2 and used the flow conditions given in Table 1. However, rather than using the digital-filtering (DF) turbulence inflow generation technique, a fully transitional boundary layer for flow over the cone was simulated. The laminar flow established at the leading edge of the cone was perturbed with acoustic waves originating in the free stream which have a frequency and wavelength close to those of the most unstable waves of the second mode instability. These perturbations then excited second mode instability waves, which amplified and rapidly broke down into fully-developed turbulence. The DNS run with the SPARC code is referred to as Case DNS SPARC in Table 2, and the details of the grid dimensions, domain size, and resolutions of Case DNS SPARC are listed in the same table.

Figure 2a shows the streamwise evolution of the skin-friction coefficient C_f for the various DNS runs and their comparison with RANS and the van Driest II theory [20]. After an initial adjustment length of approximately 0.15 m, the skin-friction prediction from the two WENO runs converges within 5% of each other and with that of the pre-cursor RANS as described in Section III.B; the skin-friction prediction with the SPARC code matches that of the laminar flow solution in the pre-transitional region and converges to the turbulent values in the downstream portion of the computational box. For the DNS WENO cases, a similar adjustment length of 0.15 m is seen for r.m.s. fluctuations of wall pressure $p'_{rms}/\overline{p}_w$ to recover from the initial transient due to the DF turbulence generation technique; the wall-pressure fluctuations of the DNS run with the SPARC code shows a large initial peak due to the breakdown of the second-mode waves and eventually converges with those of the WENO runs with 10%.

Figure 3 compares the profiles of wall-pressure power spectral density (PSD) among DNS cases at $x = 0.396$ m and $x = 0.452$ m. For all DNS cases, the wall-pressure PSD of the DNS was computed either from the "raw" wall-pressure DNS field without conducting spatial averaging (referred to as DNS $d = 0$) or from the DNS data that was spatially averaged over a circular area of diameter $d = 0.98$ mm (corresponding to the sensing area of the PCB132 transducer provided by the sensor manufacturer PCB PIEZOTRONICS, Inc.). Very good comparison in the wall-pressure spectrum is achieved over a wide range of frequencies. For spatially averaged PSD with $d = 0.98$ mm, in particular, the comparison is almost perfect among all the DNS cases. The good comparisons of pressure statistics among cases with different computational domains and inflow boundary conditions confirm that a fully developed equilibrium state of a turbulent boundary layer is achieved in selected DNS domain from $x \approx 0.4$ m until at least the base of the cone ($x \approx 0.517$ m).
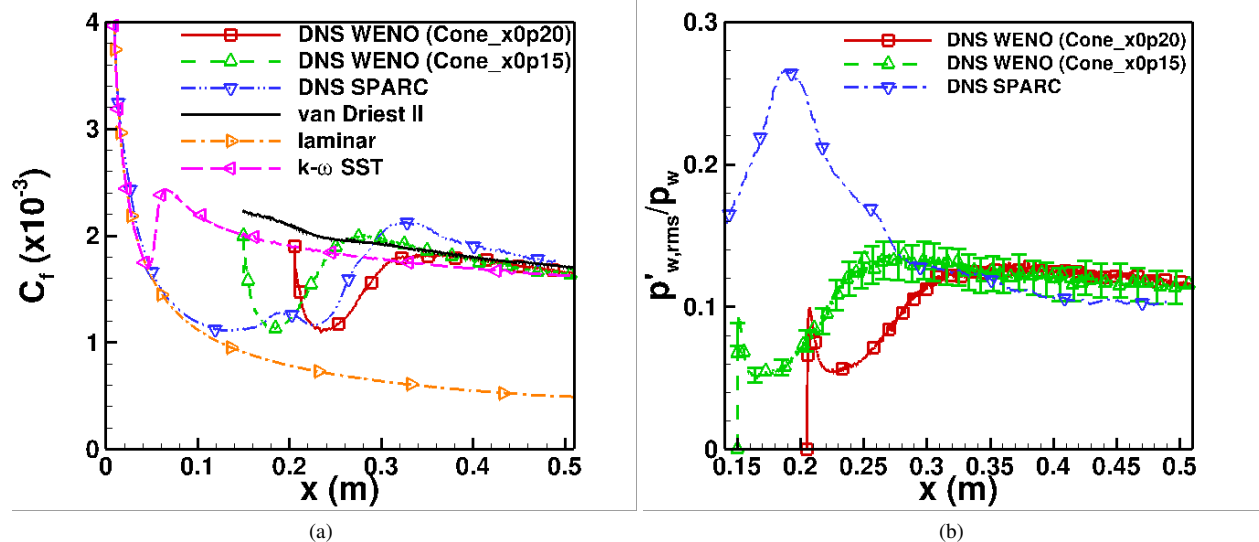
(a)

(b)

Fig. 2 Comparison of the skin-friction coefficient and the r.m.s. fluctuations of wall pressure among DNS with different computational domains and inflow boundary conditions. 10% error bars are added in the plot of the r.m.s. fluctuations of wall pressure to gauge the discrepancy in predictions of the DNS.
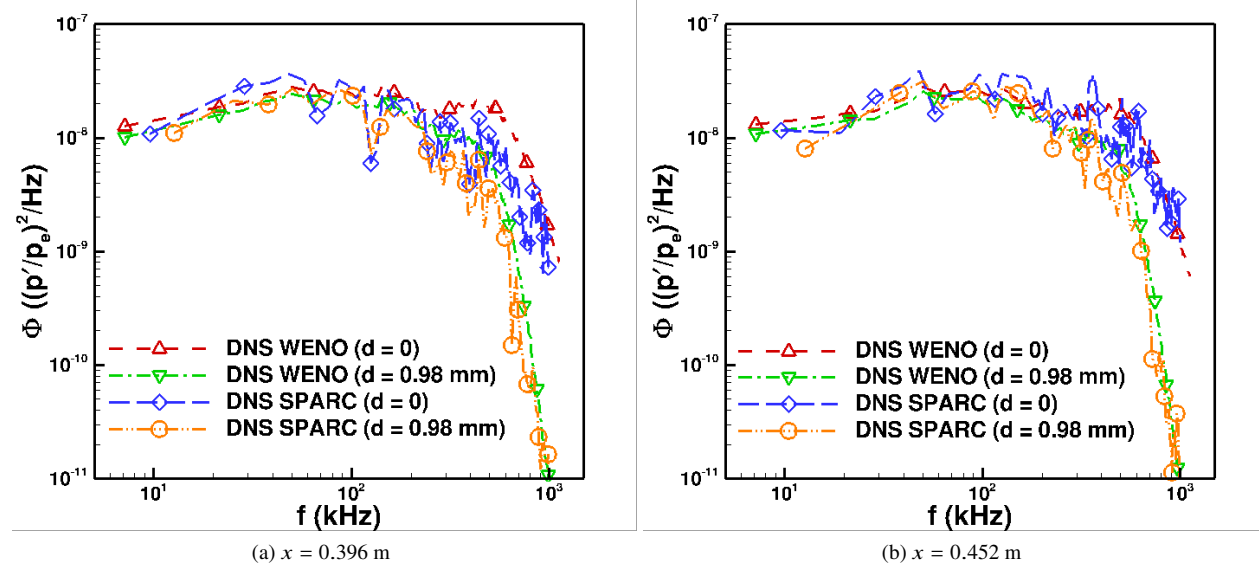

(a) $x = 0.396$ m

(b) $x = 0.452$ m

Fig. 3 Comparison of the PSD of wall-pressure fluctuations at $x = 0.396$ m and $x = 0.452$ m among DNS with different computational domains and inflow boundary conditions.

Additional validation of the current DNS is established by comparing the DNS-predicted pressure statistics with the Sandia experiments and the historical data collected by Beresh et al. [21] to be shown in Section IV.

D. A Note on DNS Averaging

In the following sections, we present the boundary-layer profiles of the WENO DNS (Case DNS_x0p15) that was computed by averaging the DNS volumetric flow-fields first in the azimuthal direction, and then in the temporal direction over 599 flow-field snapshots spanning a time interval of 1.196 ms (corresponding to approximately $419\delta/U_e$, where δ and U_e are the boundary-layer thickness and edge velocity, respectively, at a reference sensor location of $x = 0.396$) was calculated. To monitor the statistical convergence, flow statistics were computed by averaging over the whole or half the number of the flow-field snapshots, and a negligible difference ($< 1\%$) was observed between the two. Additionally, the wall-pressure PSD and coherence of the WENO DNS were calculated using surface planar time-series that were sampled at 25 MHz (corresponding to approximately $71.7U_e/\delta$); the Welch method with 16 segments were used to calculate the PSD, and the length of an individual segment is 0.14 ms (approximately $49\delta/U_e$).

The surface data from the SPARC DNS used to calculate wall-pressure statistics were sampled at 2 MHz over 0.4325 milliseconds, generating 835 data points; the Welch method with 4 segments were used to calculate PSD.

IV. Results

In this section, DNS-predicted turbulent pressure statistics over the cone geometry are first presented and compared with the Sandia experiment. In the experiment, the cone was instrumented with axial and spanwise arrays of PCB132 sensors to measure the pressure fluctuations in the boundary layer, with the sensor locations shown in Figure 4. In particular, the effect of transducer size on the wall-pressure intensity and spectrum are investigated by numerically applying spatial filtering to the DNS data, which mimics the attenuation effects resulting from the finite size of the wall-pressure transducer in the experiments. Next, the scaling relations of wall-pressure statistics and their dependence on flow configurations are investigated by comparing the characteristics of turbulent pressure fluctuations at the cone surface with those at the nozzle wall of the Sandia HWT-8 and over a flat plate at a similar freestream Mach number.

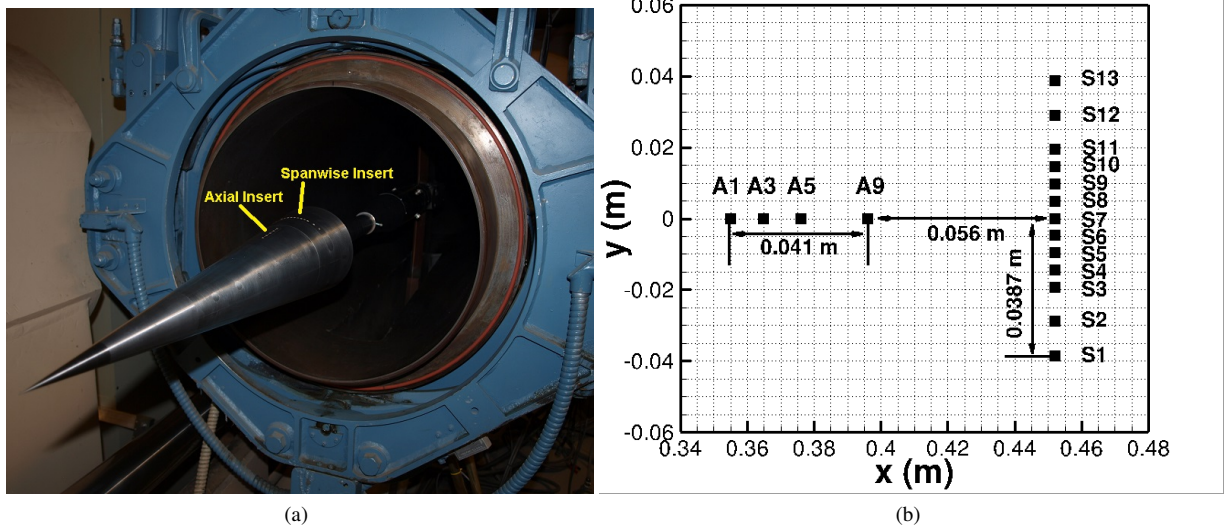(a)   (b)

Fig. 4   Schematic of locations of PCB132 sensors instrumented over the cone surface in the Sandia HWT-8. (a) Cone installed in Sandia HWT-8 (adapted from Smith et al. [3]); (b) plan view of sensor locations, wherein x **and** y **represent the streamwise and the spanwise coordinates, respectively.**

8

A. Comparison with Sandia Experiments

Figure 5 shows a comparison in wall-pressure PSD between the DNS and the Sandia's experiment at multiple axial locations of the cone. The experimental wall-pressure PSD was computed with pressure signals measured by PCB132 sensors without having been corrected per Corcos [22] for high-frequency attenuation; the wall-pressure PSD of the DNS was computed either from the "raw" wall-pressure DNS field without conducting spatial averaging (referred to as DNS $d = 0$) or from the DNS data that was spatially averaged over a circular area of diameter $d = 0.98$ mm (corresponding to $d^+ \approx 50$). The selected spatial averaging area of diameter $d = 0.98$ mm (or $d = 0.0386$ inch) is the sensing area of the PCB132 transducer provided by the sensor manufacturer PCB PIEZOTRONICS, Inc.. The PSD computed from the pressure signals measured by PCB132 shows a significantly faster spectral roll-off at high frequencies than those of the DNS without spatial averaging ($d = 0$), but a good comparison is achieved between the experimentally measured PSD and the PSD computed from the spatially-averaged DNS data with $d = 0.98$ mm. The discrepancy between DNS results with and without spatial averaging suggests that the size of the pressure transducer has caused significant attenuation at high frequencies in the experimentally measured PSD, and correction such as that per Corcos [22] with a properly selected sensing area is needed to account for such attenuation.

To illustrate the attenuation in r.m.s. wall pressure resulting from the finite transducer size, Figure 6 plots the DNS-predicted $p'_{w,rms}$ as a function of the diameter d of spatial averaging. In this figure, the experimental data points are normalized using DNS-predicted wall shear stress τ_w. A good comparison in p'_{rms} is achieved between DNS and experiments for an averaging diameter of $d = 0.98$ mm or $d = 50^+$. For an average size similar to that of a PCB132 sensor ($d = 0.98$ mm), spatial averaging causes an attenuation of approximately 27%.

In addition to the intensity and PSD of the pressure fluctuations, the coherence function represents another basic ingredient for developing statistical pressure fluctuation models. The coherence function is defined as

$$\Gamma^2(\Delta x, \Delta y, \omega) = \frac{|\Phi_{P_a P_b}(\Delta x, \Delta y, \omega)|^2}{|\Phi_{P_a P_a}(\omega)||\Phi_{P_b P_b}(\omega)|} \tag{1}$$

where $\Phi_{P_a P_b}(\Delta x, \Delta y, \omega) = \overline{\widetilde{p}^*(x, y, \omega), \widetilde{p}(x + \Delta x, y + \Delta y, \omega)}$ is the cross-power spectral density between two arbitrary points a and b separated by the distance Δx, Δy in streamwise and spanwise directions, respectively, with $\widetilde{p}$ the time-Fourier transform of the pressure fluctuations. $\Phi_{P_a P_a}(\omega)$ and $\Phi_{P_b P_b}(\omega)$ are the pressure auto-spectra at a and b, respectively.

Figure 7 plots comparisons in coherence of wall pressure fluctuations between DNS and the measurements by PCB132 sensors. The DNS-predicted coherence compares well with that of experiments for transducers with either streamwise or spanwise separations. The good comparison between the DNS without spatial filtering and the experiment suggests that the attenuation due to finite sensor sizes has only a small influence on wall-pressure coherence.

B. Effect of Flow Configurations

In this section, turbulent pressure fluctuations at the cone surface are compared with those over a Mach 8 flat plate and those at the nozzle wall of the Sandia HWT-8 to investigate wall-pressure scaling relations and the effect of flow configurations. The flat-plate and nozzle-wall results have been reported in recent papers by the present authors [12, 17, 23].

Tables 3 and 4 list flow conditions and boundary-layer properties at the selected locations for the cone, nozzle, and flat-plate configurations. All the three cases have a similar freestream Mach number of approximately 8 and a wall-to-recovery temperature of approximately 0.5, with a friction Reynolds number of $Re_\tau = 155$ for the cone case and $Re_\tau = 627$ for the nozzle case. Although Reynolds numbers may seem to be small for establishing a fully-turbulent boundary layer, Figure 8 shows that the van Driest transformed mean velocity conforms well to the incompressible law of the wall and shows a (narrow) logarithmic region, and an apparently good collapse of the Reynolds shear stress is achieved in the semilocal scaling z^* of Huang et al. [24]. Consistent with the experimental observations [3], the boundary-layer thicknesses (δ, δ^*, and θ) of the cone are more than an order of magnitude smaller than those for the nozzle wall.

Figure 9 plots the DNS data points of r.m.s wall pressure fluctuations for various flow configurations and their comparison with the historical data compiled by Beresh et al. [21]. DNS-predicted r.m.s pressure fluctuations for all the three configurations are shown to fit well with the historical test data. Figure 10 further compares the PSD of wall-pressure fluctuations among the DNS for the cone, nozzle, and flat-plate configurations. The PSD for the cone case rolls off at much higher frequencies than the other two configurations given the much smaller boundary-layer thicknesses for the cone case. An apparently good collapse of the data among the three cases is achieved via inner scaling.

(a) $x = 0.355$ m

(b) $x = 0.376$ m

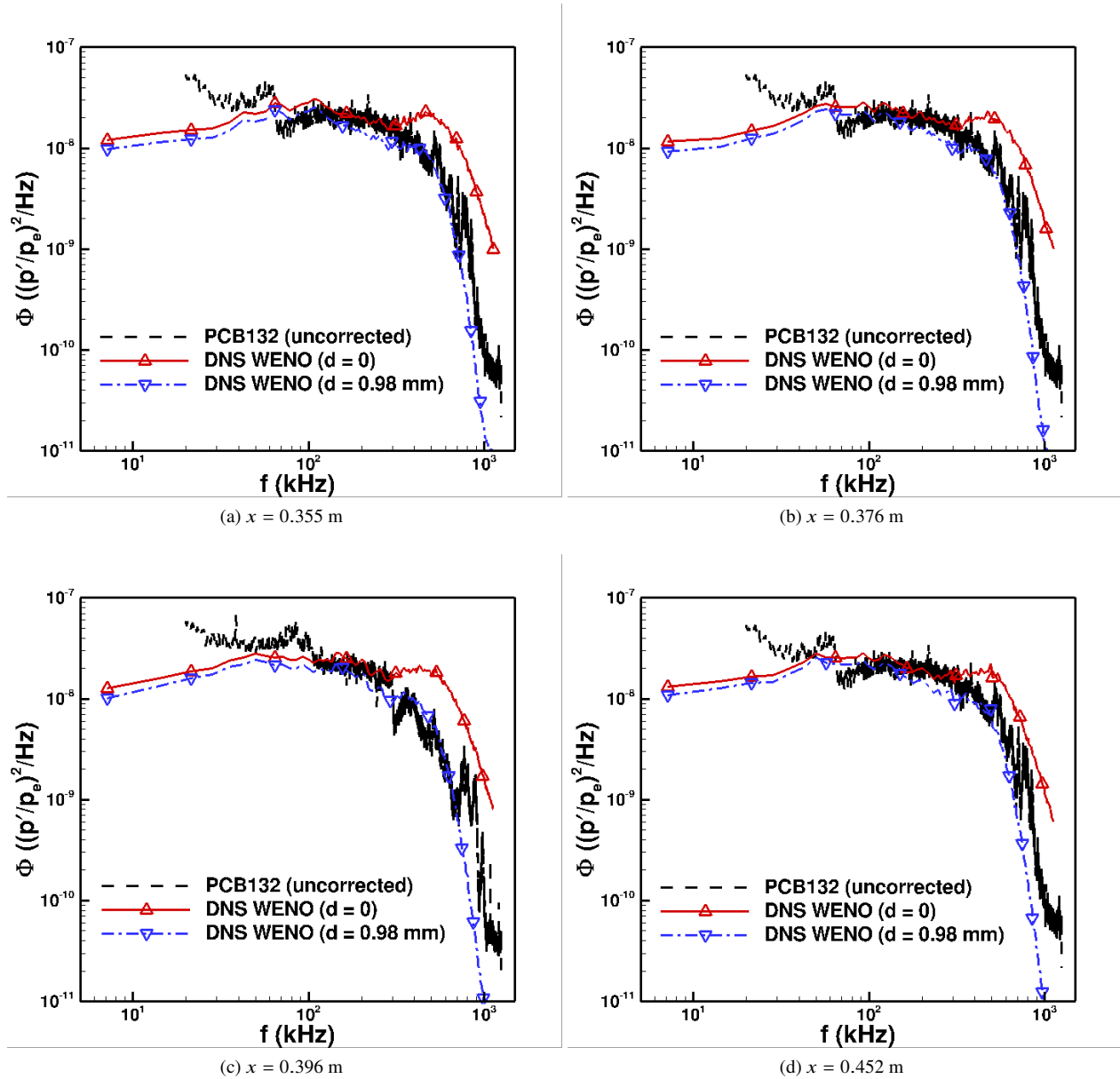(c) $x = 0.396$ m

(d) $x = 0.452$ m

Fig. 5 Comparison in wall-pressure power spectral density (PSD) at multiple axial locations of the cone between the experiment and the DNS with and without spatial averaging. The DNS data for $d = 0$ and $d = 0.98$ mm correspond to that without spatial averaging and that spatially averaged within a diameter of 0.98 mm, respectively.
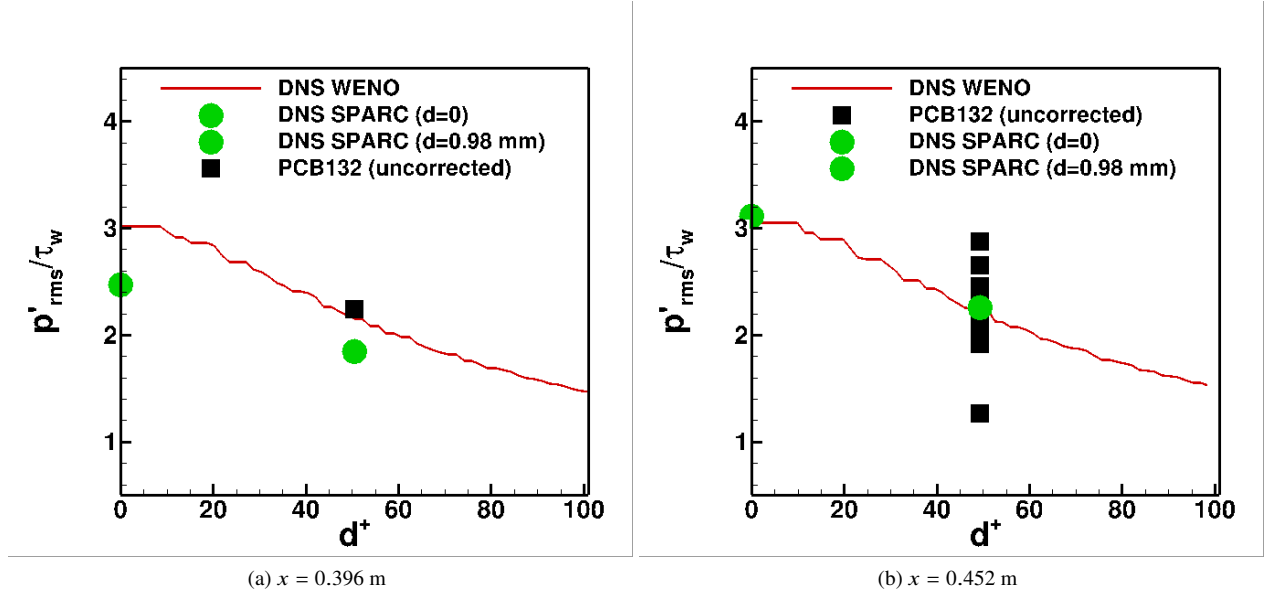
(a) $x = 0.396$ m

(b) $x = 0.452$ m

Fig. 6   The dependence of r.m.s. wall pressure on spatial-averaging diameter d.

Table 3   Freestream and boundary-layer edge conditions for various flow configurations.

Case	M_∞	$Re \times 10^6$ (1/m)	P_0 (kPa)	T_0 (K)	M_e	U_e (m/s)	q_e (kPa)	T_w (K)	T_w/T_r
Cone ($x = 0.396$ m)	7.91	13.4	4692.0	617	5.47	1046	30.7	298	0.54
Nozzle ($x = 2.336$ m)	8.07	12.2	4671.2	617	7.85	1087	19.5	298	0.54
FlatPlate	7.87	8.2	3511.5	693	6.39	1131	12.2	298	0.48

Table 4   Boundary layer properties at the reference station selected for statistical analysis for various flow configurations.

Case	Re_θ	Re_τ	H	τ_w (Pa)	u_τ (m/s)	z_τ (μm)	δ (mm)	δ^* (mm)	θ (mm)
Cone ($x = 0.396$ m)	1301	155	9.6	54.5	59.3	19.4	3.0	1.3	0.14
Nozzle ($x = 2.336$ m)	16102	627	12.5	12.8	49.9	69.5	43.6	18.2	1.45
FlatPlate	4825	418	12.2	13.1	54.2	73.6	30.8	14.5	1.18

Figures 11 and 12 show the effect of the separation distance on the streamwise and spanwise coherence of wall pressure in terms of the non-dimensional frequency $\omega\Delta x/U_c$ and $\omega\Delta y/U_c$, respectively. In the same figures, the Corcos analytical approximation [25] is reported as well. According to Corcos, the coherence function is modeled as

$$\Gamma_{ab}(\Delta x, \Delta y, \omega) = e^{-\alpha_1 \omega |\Delta x|/U_c} e^{-\alpha_2 \omega |\Delta y|/U_c} e^{i\omega\Delta x/U_c} \tag{2}$$

where the parameters α_1 and α_2 quantify the loss of coherence along the streamwise and spanwise directions, respectively; these parameters are selected by fitting the DNS data. U_c is the propagation speed calculated from the space-time correlation of wall-pressure fluctuations. For all three configurations, the Corcos model delivers good prediction of wall pressure coherence over intermediate and high frequencies but fails in the low-frequency range. A similar trend has been reported in the literature for flat-plate supersonic turbulent boundary layers [26]. Table 5 compares streamwise and spanwise decay constants of the cone, nozzle, and flat-plate configurations with those reported in the literature. The values of the streamwise decay constant (α_1) at Mach 8 are similar to those reported by Di Marco et al. at Mach 2 to
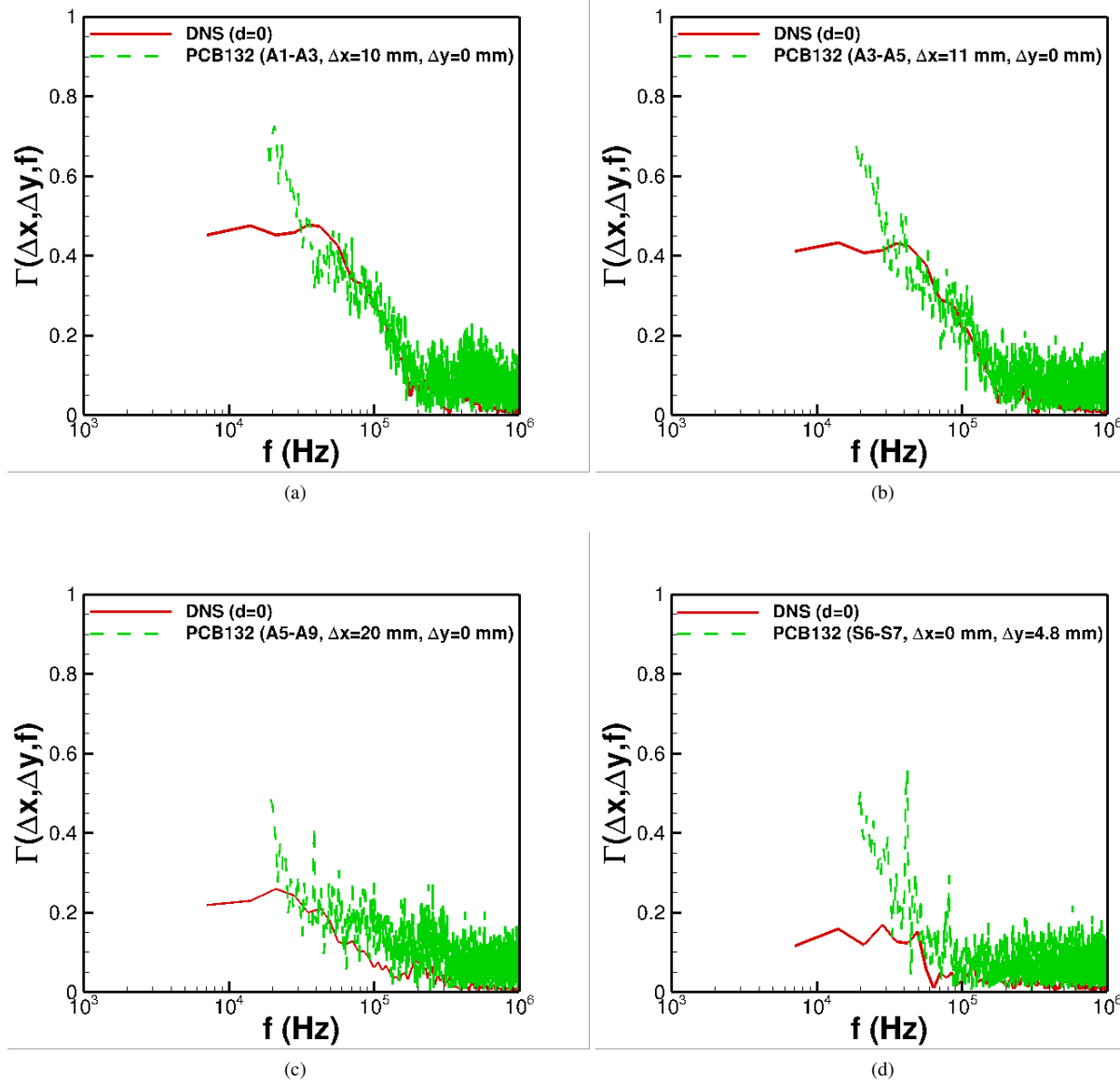
11

Fig. 7   Comparison in coherence of surface pressure fluctuations between DNS and wind-tunnel measurements.

4 [26] and those identified from the wind tunnel experiments by Beresh et al. at Mach 2 [27], while these supersonic values are significantly larger than those of the subsonic and low-speed cases [22, 28, 29]. The values of the spanwise coherence decay constant (α_2) for the three configurations at Mach 8 are similar to the low-speed and supersonic values reported in the literature.

V. Summary

This paper presented DNS of a hypersonic turbulent boundary layer developing spatially over a sharp 7° half-angle cone measured in the Sandia HWT-8. The DNS domain consisted of a section of the cone and was embedded within the domain of a pre-cursor RANS that simulated the full-cone geometry and provided boundary conditions for the DNS. Multiple DNS runs were conducted with different extents of the axial domain and inflow boundary conditions to verify the insensitivity of boundary-layer statistics to domain boundaries. Additionally, the DNS-predicted wall pressure
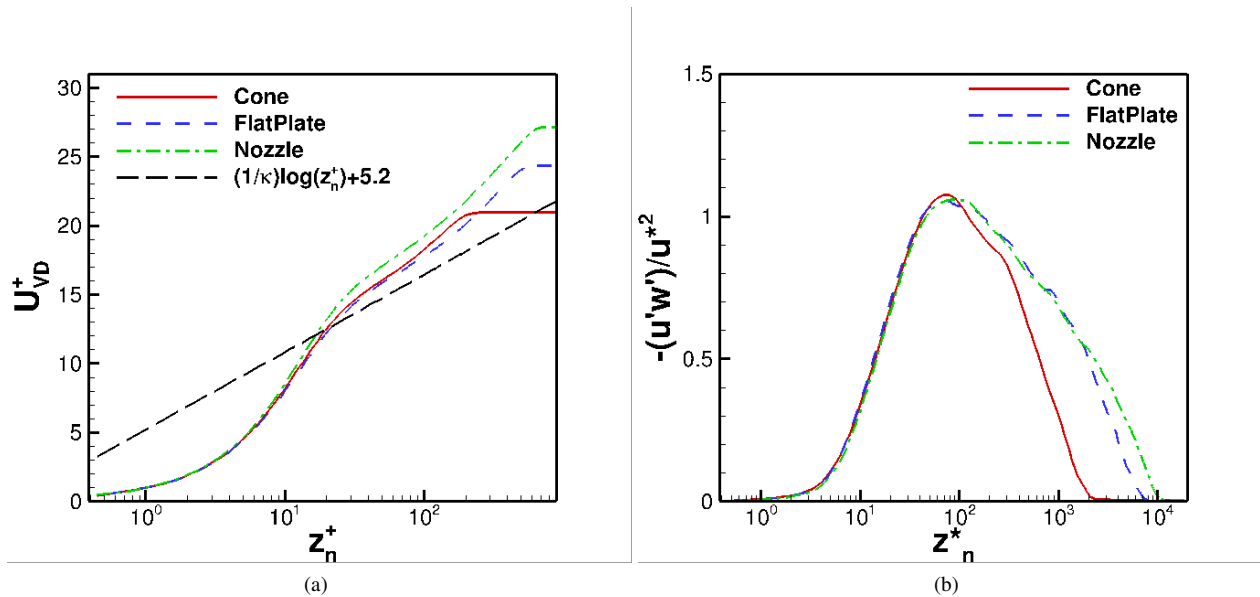
(a)

(b)

Fig. 8   Comparison of the van Driest transformed mean velocity and the normalized Reynolds shear stress among different flow configurations. $z^* = \left(\overline{\rho}(\tau_w/\overline{\rho})^{1/2}/\overline{\mu}\right)z$ **is the semilocal scaling and** $u_\tau^* = \sqrt{\tau_w/\overline{\rho}} = (\overline{\rho}_w/\overline{\rho})^{1/2}u_\tau$ **is the density weighted velocity scale.**

(a)

(b)
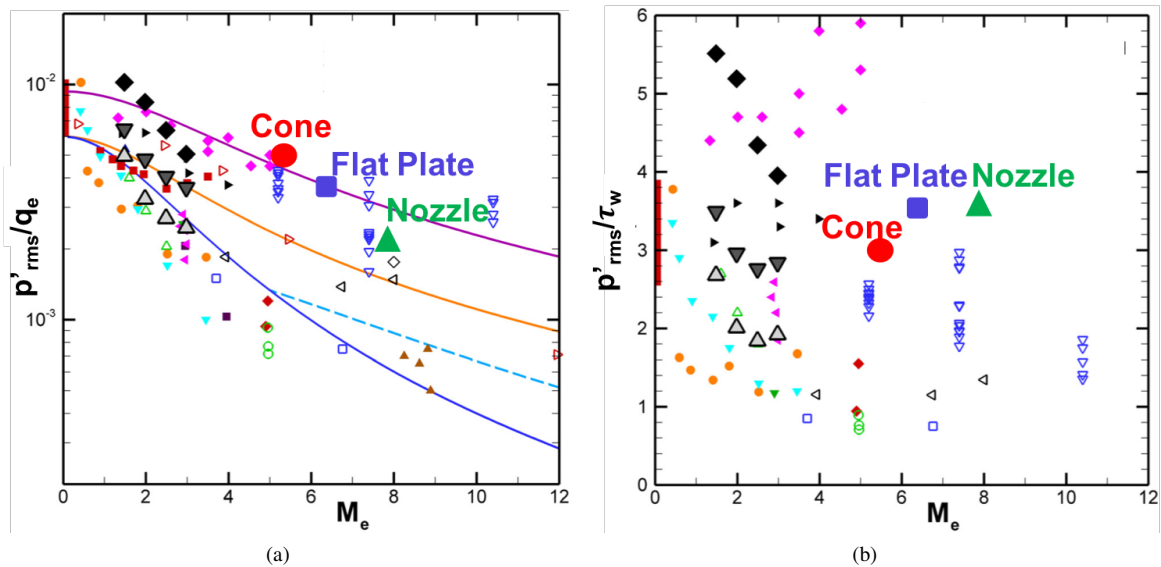
Fig. 9   r.m.s wall-pressure fluctuations for the cone, nozzle, and flat-plate configurations, normalized by: (a) dynamic pressure; (b) wall shear stress, and their comparison with the historical data compiled by Beresh et al. [21].
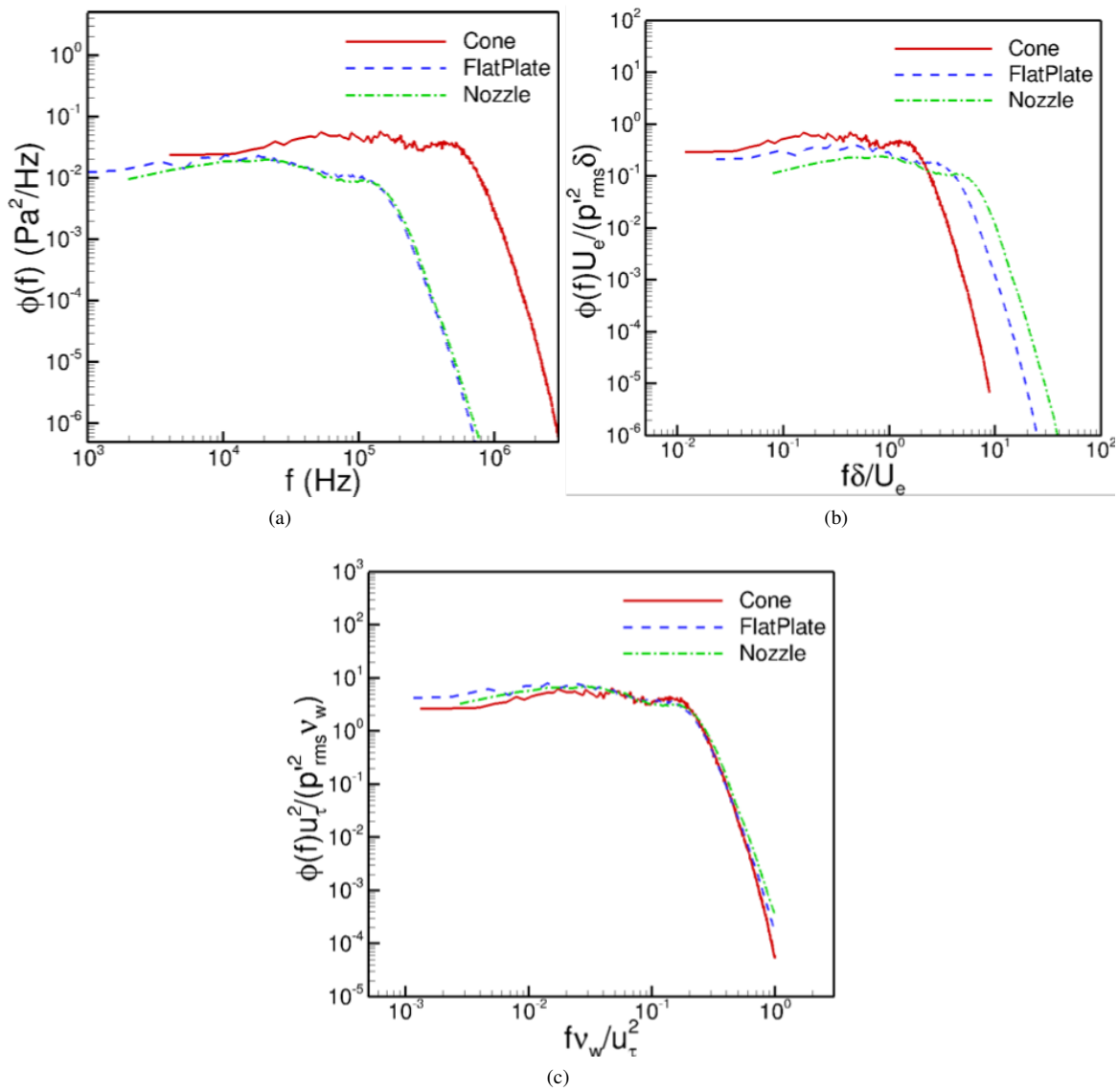
13

Fig. 10   PSD of wall-pressure fluctuations for the cone, nozzle, and flat-plate configurations.

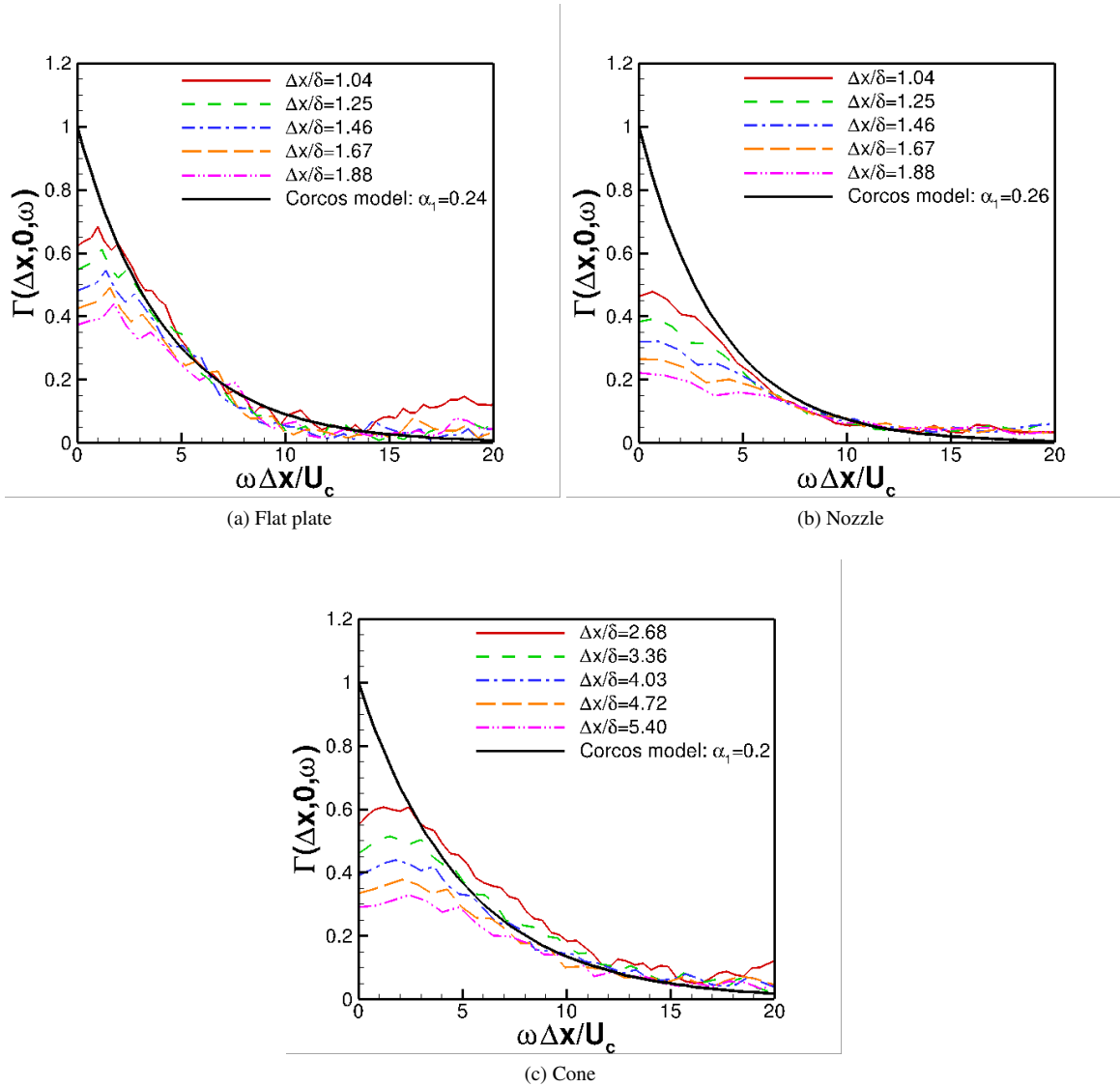(a) Flat plate

(b) Nozzle

(c) Cone

Fig. 11   Streamwise coherence as a function of the normalized frequency for cone, nozzle, and flat-plate configurations. The solid line represent the Corcos model with an exponent of α_1.
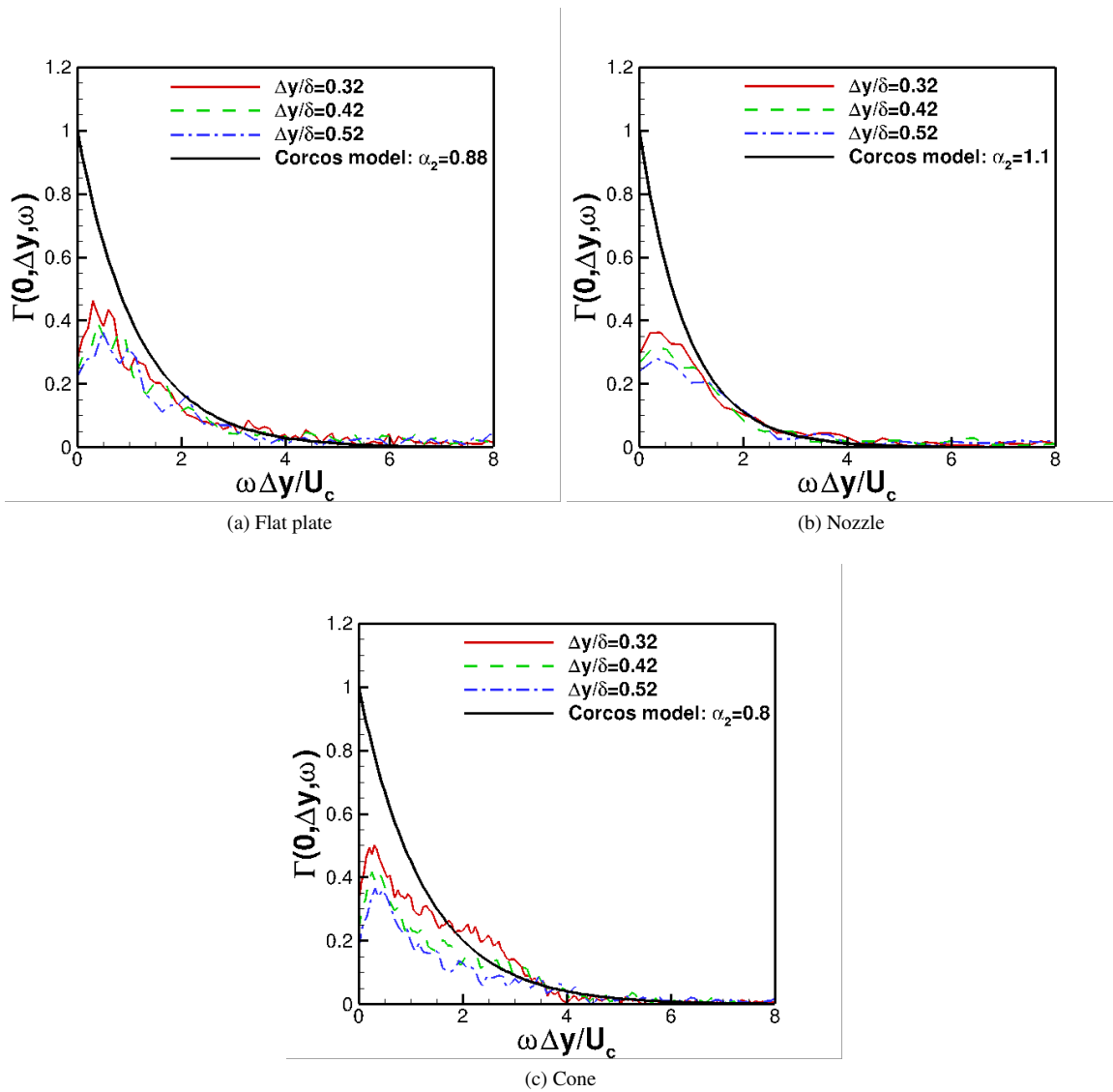
(a) Flat plate

(b) Nozzle

(c) Cone

Fig. 12   Spanwise coherence as a function of the normalized frequency for cone, nozzle, and flat-plate configurations. The solid line represent the Corcos model with an exponent of α_2.

Table 5   Corcos parameters for the streamwise and spanwise coherence evaluated for the cone, nozzle, and flat-plate configurations at Mach 8 and their comparison with those reported in the literature at lower Mach numbers.

Case	M_∞	Re_τ	α_1	α_2	U_c m/s	U_c/U_e
Cone ($x = 0.396$ m)	7.91	155	0.2	0.8	890.7	0.85
Nozzle ($x = 2.336$ m)	8.07	627	0.26	1.1	840.2	0.77
FlatPlate	7.87	418	0.24	0.88	923.4	0.82
DNS, Flat plate (by Di Marco et al. [26])	2.0	204	0.231	1.108		
	2.0	448	0.221	0.88		
	2.0	843	0.207	0.88		
	3.0	404	0.225	0.833		
	4.0	373	0.221	0.876		
Exp., Nozzle wall (by Beresh et al. [27])	2.0		$0.28 - 0.36$	0.7		
DNS, Flat plate (by Gloerfelt et al. [28])	0.5		0.12	0.72		
Exp., Flat plate (by Corcos [22])	≈ 0		0.11	0.714		
Exp., Nozzle wall (by Blake [29])	≈ 0		0.116	0.7		

statistics, including the r.m.s. fluctuations and the PSD, were validated against those measured in the Sandia HWT-8. A good comparison between the DNS and the experiment was achieved for wall-pressure PSD and r.m.s. fluctuations after spatial averaging was applied to the DNS data over an area similar to the sensing area of the transducer. The comparison between DNS and experiments showed that a finite transducer size similar to the PCB132 transducer (corresponding to $d^+ \approx 50$) caused significant spectral attenuation at high frequencies in the experimentally measured PSD, and the loss in sensor resolution resulted in an approximately 27% reduction in r.m.s. pressure fluctuations. The attenuation due to finite sensor sizes has only a small influence on wall-pressure coherence, as indicated by the good comparisons between the DNS without spatial filtering and the experiment for transducers with either streamwise or spanwise separations.

The characteristics of turbulent pressure fluctuations at the cone surface were also compared with those over a Mach 8 flat plate and at the nozzle wall of the Sandia HWT-8 to assess the effect of flow configurations on the scaling relations of turbulent pressure fluctuations. The comparison showed that the inner scaling successfully collapsed the wall-pressure PSD among the different flow configurations. For all the configurations, the Corcos model delivered good predictions of wall pressure coherence over intermediate and high frequencies but failed at low frequencies. The Corcos parameters for the streamwise and spanwise coherence at Mach 8 are similar to those predicted by DNS and experiments at lower supersonic Mach numbers [26, 27].

Acknowledgments

17

References

[1] Casper, K. M., Beresh, S. J., Henfling, J. F., Spillers, R. W., and Pruett, B. O. M., "Hypersonic Wind-Tunnel Measurements of Boundary-Layer Transition on a Slender Cone," *AIAA Journal*, Vol. 54, No. 4, 2016, pp. 1250–1263.

[2] Casper, K. M., Beresh, S. J., Wagnild, R. M., Henfling, J. F., Spillers, R. W., and Pruett, B. O. M., "Simultaneous Pressure Measurements and High-Speed Schlieren Imaging of Disturbances in a Transitional Hypersonic Boundary Layer," AIAA Paper 2013-2739, 2013.

[3] Smith, J. A., DeChant, L. J., Casper, K. M., Mesh, M., and R. V. Field, J., "Comparison of a Turbulent Boundary Layer Pressure Fluctuation Model to Hypersonic Cone Measurements," AIAA Paper 2016-4047, 2016.

[4] Keyes, F. G., "A Summary of Viscosity and Heat-Conduction Data for He, A, H_2, O_2, CO, CO_2, H_2O, and Air," *Transactions of the American Society of Mechanical Engineers*, Vol. 73, 1951, pp. 589–596.

[5] Jiang, G. S., and Shu, C. W., "Efficient Implementation of Weighted ENO Schemes," *Journal of Computational Physics*, Vol. 126, No. 1, 1996, pp. 202–228.

[6] Williamson, J., "Low-Storage Runge-Kutta Schemes," *Journal of Computational Physics*, Vol. 35, No. 1, 1980, pp. 48–56.

[7] Duan, L., Choudhari, M. M., and Wu, M., "Numerical Study of Pressure Fluctuations due to a Supersonic Turbulent Boundary Layer," *Journal of Fluid Mechanics*, Vol. 746, 2014, pp. 165–192.

[8] Duan, L., Choudhari, M. M., and Zhang, C., "Pressure Fluctuations Induced by a Hypersonic Turbulent Boundary Layer," *Journal of Fluid Mechanics*, Vol. 804, 2016, pp. 578–607.

[9] Huang, J., Zhang, C., Duan, L., and Choudhari, M. M., "Direct Numerical Simulation of Hypersonic Turbulent Boundary Layers inside an Axisymmetric Nozzle," AIAA Paper 2017-0067, 2017.

[10] Huang, J., L. Duan, L., and Choudhari, M. M., "Direct Numerical Simulation of Acoustic Noise Generation from the Nozzle Wall of a Hypersonic Wind Tunnel," AIAA Paper 2017-3631, 2017.

[11] Duan, L., Choudhari, M. M., Chou, A., Munoz, F., Ali, S. R. C., Radespiel, R., Schilden, T., Schröder, W., Marineau, E. C., Casper, K. M., Chaudhry, R. S., Candler, G. V., Gray, K. A., Sweeney, C. J., and Schneider, S. P., "Characterization of Freestream Disturbances in Conventional Hypersonic Wind Tunnels," AIAA Paper 2018-0347, 2018.

[12] Duan, L., Nicholson, G. L., Huang, J., Casper, K. M., Wagnild, R. M., and Bitter, N. P., "Direct Numerical Simulation of Nozzle-Wall Pressure Fluctuations in a Mach 8 Wind Tunnel," AIAA Paper 2019-0847, 2019.

[13] "ANSYS Fluent User Guide, Release 16.1," ANSYS Inc., 2016.

[14] Sivasubramanian, J., and Fasel, H. F., "Direct numerical simulation of transition in a sharp cone boundary layer at Mach 6: fundamental breakdown," *Journal of Fluid Mechanics*, Vol. 768, 2015, pp. 175–218.

[15] Dhamankar, N. S., Martha, C. S., Situ, Y., Aikens, K. M., Blaisdell, G. A., and Lyrintzis, A. S., "Digital Filter-Based Turbulent Inflow Generation for Jet Aeroacoustics on Non-Uniform Structured Grids," AIAA Paper 2014-1401, 2014.

[16] Huang, J., Zhang, C., and Duan, L., "Turbulent Inflow Generation for Direct Simulations of Hypersonic Turbulent Boundary Layers and their Freestream Acoustic Radiation," *AIAA Paper 2016-3639*, 2016.

[17] Duan, L., Choudhari, M. M., Chou, A., Munoz, F., Ali, S. R. C., Radespiel, R., Schilden, T., Schröder, W., Marineau, E. C., Casper, K. M., Chaudhry, R. S., Candler, G. V., Gray, K. A., and Schneider, S. P., "Characterization of Freestream Disturbances in Conventional Hypersonic Wind Tunnels," *Journal of Spacecraft and Rockets*, Vol. 56, No. 2, 2019, pp. 357–368. https://doi.org/10.2514/1.A34290.

[18] Thompson, K. W., "Time Dependent Boundary Conditions for Hyperbolic Systems," *Journal of Computational Physics*, Vol. 68, No. 1, 1987, pp. 1–24.

[19] Subbareddy, P. K., and Candler, G. V., "A fully discrete, kinetic energy consistent finite-volume scheme for compressible flows," *Journal of Computational Physics*, Vol. 228, 2009, pp. 1347–1364.

[20] Driest, E. V., "On turbulent flow near a wall," *Journal of the aeronautical sciences*, Vol. 23, No. 11, 1956, pp. 1007–1011.

[21] Beresh, S. J., Henfling, J. F., Spillers, R. W., and Pruett, B. O. M., "Fluctuating Wall Pressures Measured beneath a Supersonic Turbulent Boundary Layer," *Physics of Fluids*, Vol. 23, No. 7, 2011.

[22] Corcos, G., "Resolution of pressure in turbulence," *The Journal of the Acoustical Society of America*, Vol. 35, No. 2, 1963, pp. 192–199.

[23] Zhang, C., Duan, L., and Choudhari, M. M., "Direct numerical simulation database for supersonic and hypersonic turbulent boundary layers," *AIAA Journal*, Vol. 56, No. 11, 2018, pp. 4297–4311.

[24] Huang, P. G., Coleman, G. N., and Bradshaw, P., "Compressible Turbulent Channel Flows: DNS Results and Modelling," *Journal of Fluid Mechanics*, Vol. 305, 1995, pp. 185–218.

[25] Corcos, G. M., "The Structure of the Turbulent Pressure Field in Boundary-Layer Flows," *Journal of Fluid Mechanics*, Vol. 18, 1964, pp. 353–378.

[26] Di Marco, A., Camussi, R., Bernardini, M., and Pirozzoli, S., "Wall Pressure Coherence in Supersonic Turbulent Boundary Layers," *Journal of Fluid Mechanics*, Vol. 732, 2013, pp. 445–456.

[27] DeChant, L. J., and Smith, J. A., "Band Limited Correlation Estimates for $A(\xi\omega/U)$ and $B(\eta\omega/U)$ Using Beresh et. al. 2013 Data Sets," Tech. rep., SAND2014-1123, 2014.

[28] Gloerfelt, X., and Berland, J., "Turbulent boundary-layer noise: direct radiation at Mach number 0.5," *Journal of Fluid Mechanics*, Vol. 723, 2013, pp. 318–351.

[29] Blake, W. K., "Turbulent boundary-layer wall-pressure fluctuations on smooth and rough walls," *Journal of Fluid Mechanics*, Vol. 44, No. 4, 1970, pp. 637–660.